Journal of Computational and Applied Mathematics 428 (2023) 115165

Contents lists available at ScienceDirect

Journal of Computational and Applied Mathematics

journal homepage: www.elsevier.com/locate/cam

On effects of concentrated loads on perforated sensitive shells of revolution

Stefano Giani [a], Harri Hakula [b,*]

[a] Durham University, School of Engineering and Computing Sciences, South Road, Durham, DH1 3LE, United Kingdom
[b] Aalto University, Department of Mathematics and System Analysis, P.O. Box 11100, FI–00076 Aalto, Finland

ARTICLE INFO

Article history:
Received 31 October 2022
Received in revised form 9 February 2023

MSC:
65C20
65N12
65N25
65N30

Keywords:
Concentrated loads
Sensitivity
Perforations
Shells of revolution

ABSTRACT

Sensitive shells are a class of constructions with specific and perhaps unintuitive responses to different loading scenarios. There are new emerging applications for capsules with open cavities, and as the designs are optimised to maximise the payload, sensitivity has to be taken into account. Concentrated loads induce singularities that propagate along the characteristics of the surfaces. Perforation patterns do not have a strong effect on internal layers. Under a symmetric concentrated loads for parabolic and hyperbolic shells there exists a critical thickness at which local features of solution begin to dominate, whereas for elliptic cases there is always a dominant global response. In non-uniform curvature cases the elliptic part will dictate the solution even if the load is not acting on it. The extensive set of simulations has been computed using high-order finite element solvers including adaptivity.

1. Introduction

Shells of revolution are often containers, for instance, pressure vessels. An immediate consequence of maximisation of the payload volume under external volume constraints is the need to make the walls of the containers as thin as possible. In this paper we consider a very specific class of containers designed for future medical applications, namely optionally biodegradable, preferably perforated capsules used for long-term drug delivery inside human bodies (see, for instance, the excellent paper by Auvinen et al. [1]). Currently there are many open questions concerning realistic designs. In Fig. 1 three schematics for prototypes of monolithic, reservoir-type implants are shown. Auvinen reports on samples with a length of 2 cm and volume of 400 mm^3 which are not yet thin due to limitations of the chosen manufacturing process, namely, 3D printing. However, printed nanocellulose sheets have already been reported to have thicknesses in the μm range [2]. In this study we assume that linear elasticity remains valid and the material is metal, for instance, medical grade titanium.

In the proposed designs the payload is an injectable drug-releasing hydrogel formulation. The drug release rate is modulated by a led device, which in mechanical terms is an attached solid at one end of the shell. The hydrogels are shear thinning and, therefore, it is reasonable not to include fluid–structure interactions into the model. As the drugs are released from the gel, they simply leak out from the open end or possible perforations. When in use, the capsules are subject to external pressure loading, which can be assumed to be uniform under normal circumstances. However, of concern are different impact loads during the use and process of insertion and possibly removal for reuse [3]. The expected drug release rate is based on the ideal shape of the open end of the capsule [1].

* Corresponding author.
E-mail addresses: stefano.giani@durham.ac.uk (S. Giani), Harri.Hakula@aalto.fi (H. Hakula).

https://doi.org/10.1016/j.cam.2023.115165

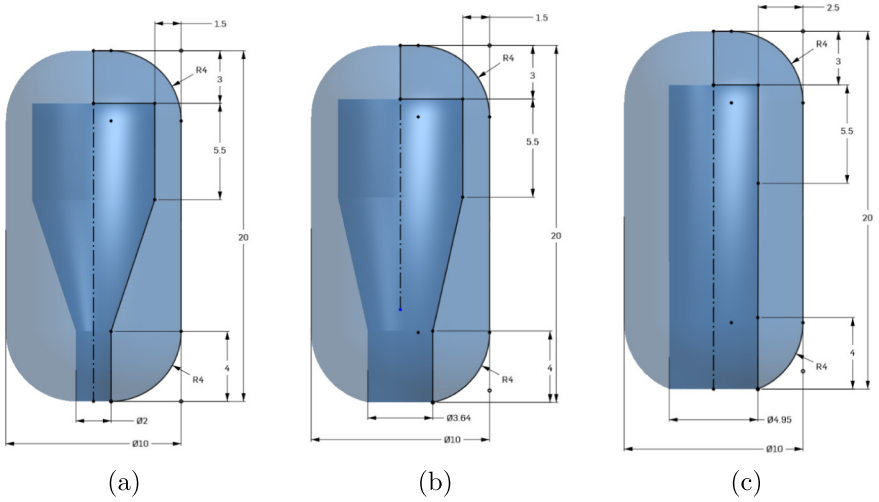

Fig. 1. Three realistic capsule designs with the limit payload regions indicated. Designs (a) and (b) have non-uniform curvature inner shells, (c) is a cylinder.
Source: Images courtesy of V. Auvinen/University of Helsinki.

A fascinating, shell-specific feature emerges when only one end of the capsule is sealed completely while the other one is either open or otherwise only lightly kinematically constrained. The shell structure is said to be sensitive in this case, and famously the elliptic shells lose coercivity as the dimensionless thickness tends to zero leading to large displacements. More precisely, the Shapiro–Lopatinsky conditions are not satisfied in the limit. The book by Sanchez-Palencia [4] is a comprehensive treatise on this topic. The existing theory is limited in the sense that the exact analysis inherently assumes that the variation of the shell profile is uniform in some well-defined way; for instance, the type of the Gaussian curvature does not change. If this assumption does not hold, simulation is the only option available. This is the situation with respect to designs of Figs. 1(a) and 1(b).

Concentrated loads or point loads are interesting in the context of shell structures since the concentrated loads excite singularities that propagate along the characteristics of the surface. In fact, these characteristics act as boundary layer generators, where the layers can indeed be internal layers as well. Elliptic surfaces cannot have internal layers, yet, if the elliptic shell is sensitive, the effect of the concentrated load is global, that is, the deformations are not confined to some well-defined subregions of the surface. To our knowledge, the effect of perforations to either the propagation of singularities or sensitive structures has not been discussed in the literature before. The choice of the loading types and locations is based on our earlier work on related eigenproblems, [5,6]. It is now established that the effects along the perforated areas and non-perforated ones depend on the dimensionless thickness with the local effects eventually dominating as the dimensionless thickness tends to zero.

1.1. Novelty of this work

This work is computational in nature since tools for mathematical analysis of these rather complex structures are not readily available. With carefully designed experiments spanning reasonable parameter space, we can derive conjectures and demonstrate the effects of perforations when compared with the reference structures. There are three observations that form the main results.

A regular perforation pattern or a $g \times g$-grid of holes divides the shell surface into regions (rows) with holes and without. On parabolic shells the loads acting on perforated regions or rows will eventually as $t \to 0$ have stronger deflection amplitudes than those acting on the regions without holes as the dimensionless thickness tends to zero. This means that there exists a critical thickness t_c below which the local features due to boundary and internal layers dominate the solution, and for instance effectively make simple homogenisation impractical.

For hyperbolic shells the standout feature is the interesting superposition of the internal layers at their crossings. The concentrated loads induce singularities that propagate along the characteristics of the surface. With symmetric loading it is possible that two sets of internal layers cross and through superposition create regions of stronger deflections that can lie far from the point of loading.

It is not surprising that the sensitivity of elliptic shells is present also in perforated cases. In the mixed geometry, i.e., non-uniform curvature type, case even though the load is not acting on the elliptic region, the propagation of singularities reaching that region is enough to excite a very energetic response.

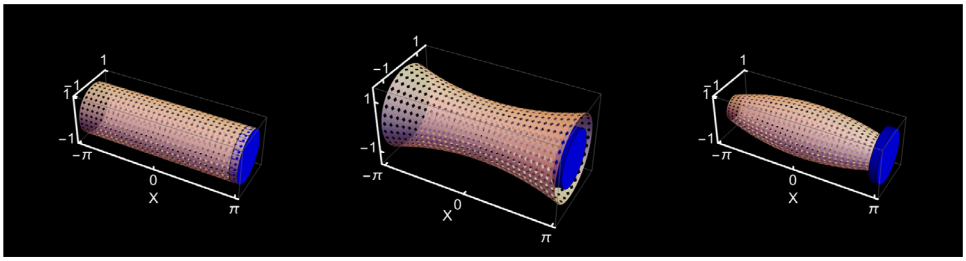

Fig. 2. Shell geometries. From left: Parabolic, hyperbolic, elliptic. The blue disc represents the possible blue light source and acts as a visual reference.

1.2. Brief review of literature

For sensitive shells the case of pressure loading was considered by Pitkäranta and Sanchez-Palencia [7], and symmetric concentrated loading by Bathe and al. [8]. Sensitivity has also been touched on in the context of eigenproblems, first in [9] and later comprehensively in [10]. Shell structures are also sensitive to imperfections (material or geometric), a problem class which is related yet different from the much narrower range of effects discussed here. For a concise introduction to broader issues related to imperfections, see [11]. In the future, once more experimental data are available, one should consider stochastic analysis where the variation in the curvature is included [12].

The accurate description of the shell geometry is central since, ultimately, the interesting effects are geometry-dependent. There are many shell models to choose from. In recent years, isogeometric analysis [13] has been promoted as the modern method of choice. From the analysis point-of-view, a much simpler, the so-called mathematical shell model by Pitkäranta [14] also called the shallow shell model, is sufficient for the uniform curvature type cases. An additional model used here is a variant of the Naghdi model [15] for shells of revolution. Using the formulation by Malinen [16], the geometry is also exact as in the isogeometric case. Sanchez-Palencia's analysis is based on the Koiter model, which requires C^1 finite elements [4].

Any computational study on shells has to account for numerical locking. Within the context of this work, numerical locking is understood as the inevitable loss of the optimal convergence rate [17,18]. No attempts to modify the underlying variational formulation have been made; the loss of the convergence rate is compensated by high-order finite elements, i.e., the *hp*-version of the FEM [19,20] and adaptivity. Adaptivity was also used by Sanchez-Palencia [4]. Other approaches for the general case would be to treat the formulation directly [21] or use well-tuned low-order elements [22,23].

1.3. Structure of the discussion

The necessary shell models are introduced in Section 2. The layer structures and the effects of perforation patterns are reviewed in Section 3. Section 4 covers solvers and numerical locking. The extensive set of numerical experiments is presented in Section 5 followed by conclusion in the final section.

2. Models

2.1. Designs

Sensitive shells are not common in engineering since their performance is highly dependent on the geometry of the shell. Each shell is a three-dimensional structure with a thickness d. In analysis and computations, the dimensionless thickness $t = d/L$, where L is typically the diameter of the domain, is used instead. This means that usually the current practical range of dimensionless thicknesses is taken as $[10^{-3}, 10^{-2}]$, where the upper limit is determined by the dimension reduction and not by the material properties. Here, in light of recent material developments we push for $[10^{-4}, 10^{-2}]$. The solutions to shell problems can often be viewed as linear combinations of local solutions with characteristic length scales that depend on the dimensionless thickness and the local curvature of the shell. Hence it is useful to define the shell surfaces (or parts of them) as either parabolic, hyperbolic, or elliptic. Refer to Fig. 2 for examples.

A shell of revolution is defined by the profile function $f(x)$ defined over some interval $x \in I = [x_0, x_1]$ which rotates around the axis of revolution, which, without any loss of generality, is the x-axis in the sequel. Using the derivatives of the profile function we can classify all shell geometries in terms of Gaussian curvature (see, for instance, [24]). The analysis of shell problems is greatly simplified if the type of curvature is uniform. In the present study, even though this condition does not hold, the classification remains meaningful locally.

1 Parabolic (Zero Gaussian curvature shells). $f''(x) = 0, \ \forall\, x \in I$.
2 Elliptic (Positive Gaussian curvature shells). $f''(x) < 0, \ \forall\, x \in I$.
3 Hyperbolic (Negative Gaussian curvature shells). $f''(x) > 0, \ \forall\, x \in I$.

2.2. Dimensionally reduced elasticity equations

Consider a shell of (constant) thickness d, the mid-surface ω of which occupies a region to of some smooth surface Γ. This is a three-dimensional body for which the 3D theory of linear elasticity could be considered 'exact' for small deformations. However, we apply here one of the classical dimension reduction models, since these models reveal the nature of shell deformations more explicitly. Such models are often reasonably accurate for thin shells [14]. The model we consider is one of the most popular models in finite element computations. Here the displacement field $\mathbf{u}$ has five components u, v, w, θ, ψ, each of which is a function of two variables on the mid-surface of the shell. The first two components represent the tangential displacements of the mid-surface, w is the transverse deflection, and θ, ψ are dimensionless rotations. The model is similar to the Reissner–Mindlin model for plate bending and is sometimes named after Naghdi. Assume that the shell consists of homogeneous isotropic material with Young modulus E and Poisson ratio ν. Then the total energy of the shell in our dimension reduction model is expressed as

$$\mathcal{F}(\mathbf{u}) = \frac{1}{2} D(a(\mathbf{u},\mathbf{u}) + d^2\, b(\mathbf{u},\mathbf{u})) - q(\mathbf{u}), \tag{1}$$

where $D = E\,d/(12(1-\nu^2))$ is a scaling factor (see for instance [25]), q is the external load potential, and $a(\mathbf{u},\mathbf{u})$ and $b(\mathbf{u},\mathbf{u})$ represent the portions of total deformation energy that are stored in membrane and transverse shear deformations and bending deformations, respectively. The latter are quadratic forms independent of d and defined as

$$\begin{aligned} a(\mathbf{u},\mathbf{u}) &= a_m(\mathbf{u},\mathbf{u}) + a_s(\mathbf{u},\mathbf{u}) \\ &= 12\int_\omega \Big[\nu(\beta_{11}(\mathbf{u})+\beta_{22}(\mathbf{u}))^2 + (1-\nu)\sum_{i,j=1}^{2}\beta_{ij}(\mathbf{u})^2\Big] A_1A_2\; d\gamma \\ &\quad + 6(1-\nu)\int_\omega \Big[(\rho_1(\mathbf{u})^2 + \rho_2(\mathbf{u}))^2\Big] A_1A_2\; d\gamma, \end{aligned} \tag{2}$$

$$b(\mathbf{u},\mathbf{u}) = \int_\omega \Big[\nu(\kappa_{11}(\mathbf{u})+\kappa_{22}(\mathbf{u}))^2 + (1-\nu)\sum_{i,j=1}^{2}\kappa_{ij}(\mathbf{u})^2\Big] A_1A_2\; d\gamma, \tag{3}$$

where β_{ij}, ρ_i, and κ_{ij} stand for the membrane, transverse shear, and bending strains, respectively. The strain–displacement relations are linear and involve at most first derivatives of the displacement components. The principal curvature coordinates, where there are only four parameters, the radii of principal curvature R_1, R_2, and the so-called Lamé parameters, A_1, A_2, which relate coordinate changes to arc lengths, are needed to specify the curvature and the metric on Γ. Here

$$A_1(x) = \sqrt{1+[f'(x)]^2}, \qquad A_2(x) = f(x), \tag{4}$$

and

$$R_1(x) = -\frac{A_1(x)^3}{f''(x)}, \qquad R_2(x) = A_1(x)A_2(x). \tag{5}$$

Using the identities above, the bending, membrane, and shear strains [16], κ_{ij}, β_{ij}, and ρ_i, respectively, can be written as

$$\begin{aligned} \kappa_{11} &= \frac{1}{A_1}\frac{\partial\theta}{\partial x} + \frac{\psi}{A_1A_2}\frac{\partial A_1}{\partial y}, \\ \kappa_{22} &= \frac{1}{A_2}\frac{\partial\psi}{\partial y} + \frac{\theta}{A_1A_2}\frac{\partial A_2}{\partial x}, \\ \kappa_{12} &= \kappa_{21} = \frac{1}{2}\Bigg[\frac{1}{A_1}\frac{\partial\psi}{\partial x} + \frac{1}{A_2}\frac{\partial\theta}{\partial y} - \frac{\theta}{A_1A_2}\frac{\partial A_1}{\partial y} - \frac{\psi}{A_1A_2}\frac{\partial A_2}{\partial x} \\ &\quad - \frac{1}{R_1}\left(\frac{1}{A_2}\frac{\partial u}{\partial y} - \frac{v}{A_1A_2}\frac{\partial A_2}{\partial x}\right) \\ &\quad - \frac{1}{R_2}\left(\frac{1}{A_1}\frac{\partial v}{\partial x} - \frac{u}{A_1A_2}\frac{\partial A_1}{\partial y}\right)\Bigg], \end{aligned}$$

$$\begin{aligned} \beta_{11} &= \frac{1}{A_1}\frac{\partial u}{\partial x} + \frac{v}{A_1A_2}\frac{\partial A_1}{\partial y} + \frac{w}{R_1}, \\ \beta_{22} &= \frac{1}{A_2}\frac{\partial v}{\partial y} + \frac{u}{A_1A_2}\frac{\partial A_2}{\partial x} + \frac{w}{R_2}, \\ \beta_{12} &= \beta_{21} = \frac{1}{2}\left(\frac{1}{A_1}\frac{\partial v}{\partial x} + \frac{1}{A_2}\frac{\partial u}{\partial y} - \frac{u}{A_1A_2}\frac{\partial A_1}{\partial y} - \frac{v}{A_1A_2}\frac{\partial A_2}{\partial x}\right), \end{aligned}$$

$$\rho_1 = \frac{1}{A_1}\frac{\partial w}{\partial x} - \frac{u}{R_1} - \theta,$$
$$\rho_2 = \frac{1}{A_2}\frac{\partial w}{\partial y} - \frac{v}{R_2} - \psi.$$

Remark 1. When the shell parametrisations defined above are used, all terms of the form $\partial A_i/\partial y$ are identically zero.

The energy norm $|||\cdot|||$ is defined in a natural way in terms of the deformation energy:

$$\mathcal{E}(\mathbf{u}) := |||\mathbf{u}|||^2 = a(\mathbf{u},\mathbf{u}) + d^2\, b(\mathbf{u},\mathbf{u}). \tag{6}$$

Similarly for bending, membrane, and shear energies:

$$B(\mathbf{u}) := d^2\, b(\mathbf{u},\mathbf{u}), \qquad M(\mathbf{u}) := a_m(\mathbf{u},\mathbf{u}), \qquad S(\mathbf{u}) := a_s(\mathbf{u},\mathbf{u}). \tag{7}$$

The load potential has the form

$$q(\mathbf{v}) = \int_\omega \mathbf{f}(x,y)\cdot\mathbf{v}\, A_1 A_2\, dx\, dy.$$

We are interested in problems where the load acts either in the transverse direction of the shell surface, i.e., $\mathbf{f}(x,y) = [0,0,f_w(x,y),0,0]^T$, or axially, $\mathbf{f}(x,y) = [f_u,0,0,0,0]^T$. It can be shown that if for the load $\mathbf{f} \in [L^2(\omega)]^5$ holds, the variational problem has a unique weak solution $\mathbf{u} \in [H^1(\omega)]^5$. The corresponding result is true in the finite dimensional case, when the finite element method is employed.

The existence of the asymptotic displacement field corresponding to the limit $t \to 0$ is possible if a suitable scaling of the load amplitude is done in the limit process. For discussion on details, see Malinen and Pitkäranta [26].

2.3. Mathematical shell model

In the following we will simplify the model by assuming that ω is a domain expressed in the coordinates x and y. Furthermore, we assume that the curvature tensor $\{b_{ij}\}$ of the midsurface is constant and write $a = b_{11}, b = b_{22}$, and $c = b_{12} = b_{21}$. The shell is then called elliptic when $ab - c^2 > 0$, parabolic when $ab - c^2 = 0$, and hyperbolic when $ab - c^2 < 0$. The above assumptions are valid for example when the shell is shallow, i.e. the midsurface differs only slightly from a plane. In the simplest case one may set $\mathrm{d}\omega = \mathrm{d}x\mathrm{d}y$ and write the relation between the strain and the displacement fields as

$$\begin{aligned}
&\beta_{11} = \frac{\partial u}{\partial x} + aw, \qquad \beta_{22} = \frac{\partial v}{\partial y} + bw, \qquad \beta_{12} = \frac{1}{2}\left(\frac{\partial u}{\partial y} + \frac{\partial v}{\partial x}\right) + cw,\\
&\rho_1 = \theta - \frac{\partial w}{\partial x}, \qquad \rho_2 = \psi - \frac{\partial w}{\partial y},\\
&\kappa_{11} = \frac{\partial \theta}{\partial x}, \qquad \kappa_{22} = \frac{\partial \psi}{\partial y}, \qquad \kappa_{12} = \frac{1}{2}\left(\frac{\partial \theta}{\partial y} + \frac{\partial \psi}{\partial x}\right).
\end{aligned} \tag{8}$$

This choice of shell model gives us additional flexibility in the design of the numerical experiments since the model admits *non-realisable* shell geometries. This is due to the assumption that the local curvatures are constant at every point of the surface.

Remarkably, for parabolic shells these strains differ from those of the standard Naghdi model only in κ_{12} and ρ_1, when the radius is $= 1$. Naturally, for non-parabolic geometries the differences are much more extensive. Notice, that the resulting system has constant coefficients which simplifies the implementation of the model significantly.

3. Propagation of singularities within perforations

In shells singularities are propagated along the characteristics of the surfaces. These local features of the solution have a characteristic length scale which is a function of the dimensionless thickness t. This is immediately visible in plots of Figs. 4 where a symmetric concentrated load has been applied at the free boundary as an axial pull, that is, it is acting on the u-component. For the parabolic and hyperbolic examples the internal layers emerge as expected. However, there are no characteristics lines on elliptic surfaces, yet at the boundary a clearly parameter-dependent feature can be seen. The exact predicted scales are given in Table 1 and visualised in Fig. 3.

For elliptic shells in this configuration the response at the boundary is an oscillation with a parameter-dependent wave number. Moreover, the local amplitudes are orders of magnitude larger than those in corresponding parabolic and hyperbolic ones. This is the origin of the term "sensitive" in this context.

Table 1
Characteristic length scales.

Geometry	Boundary layer	Internal layer	Boundary oscillation
Parabolic	t, $\sqrt{t}$	$\sqrt[4]{t}$	–
Hyperbolic	t, $\sqrt{t}$	$\sqrt[3]{t}$	–
Elliptic	t, $\sqrt{t}$	–	$K \sim -\log t$

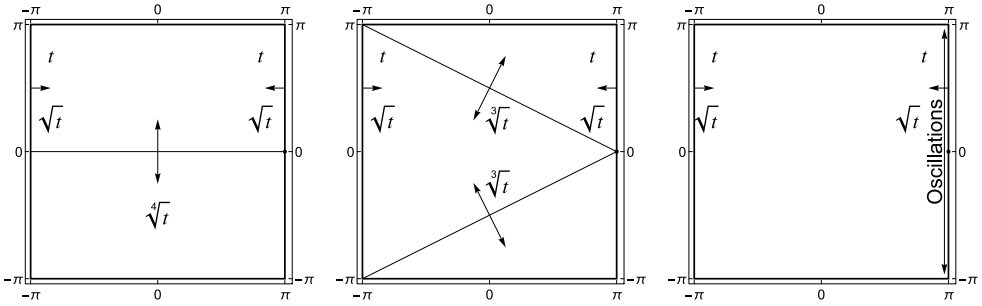

(a) Parabolic. (b) Hyperbolic. (c) Elliptic.

Fig. 3. Layer charts for different geometries. The concentrated load is assumed to act at the centre of the right hand side boundary with the left one clamped. The arrows indicate the direction in which the width of the layer varies. There are no internal layers in the elliptic problems.

3.1. Perforations

In Figs. 5 and 6 the transverse deflections of the same configurations are shown on regular and triangular perforation patterns, and with deformations, respectively. It is important to notice that the propagation of singularities is not analogous to wave propagation. The perforation patterns do not have a strong effect on the characteristic length scales. However, in the sequel it becomes apparent that the response depends on how the characteristic lines emanate from the point at which the concentrated load acts.

3.2. Shell models

One additional component affecting the analysis of the behaviour of the solutions is the chosen shell model. Here both Naghdi and shallow shell model are used. The shallow shell model is Naghdi-like in the sense that even the short t scale is accounted for but in asymptotic analysis with $t \to 0$ the constants of convergence are different between the two models. Also, the constant curvature assumption built-in to the shallow shell model leads to geometric consistency error in hyperbolic and elliptic cases.

4. High-order finite element method solvers

All numerical simulations reported here have been computed with two different high-order continuous Galerkin codes in 2D solving the variational formulation on conforming meshes of triangular elements.

4.1. Numerical locking

One of the challenges in shell problems is to avoid numerical locking. Here, one has to let the higher-order FEM alleviate the locking and accept that some thickness dependent error amplification or locking factor, $K(t) \geq 1$, is unavoidable. For the *hp*-FEM solution one can derive a simple error formulation

$$\text{error} \sim K(t)(h/L)^p, \tag{9}$$

where h is the mesh spacing, L is the diameter of the domain, and p is the degree of the elements. It is possible that $K(t)$ diverges as t tends to zero, with the worst case being for pure bending problems: $K(t) \sim 1/t$. Of course, for $K(t) \sim 1$ one can expect the *hp*-solution to be optimal in the sense of approximation theory. This simple error formula also suggests why higher-order methods are advantageous in shell problems: the mesh over-refinement in the "worst" case is $\sim (1/t)^{1/p}$, which for a fixed $t = 1/100$, say, indicates that for $p = 4$ the requirement is moderate in comparison to the case of $p = 1$. For a more detailed discussion on this and further references, see [18].

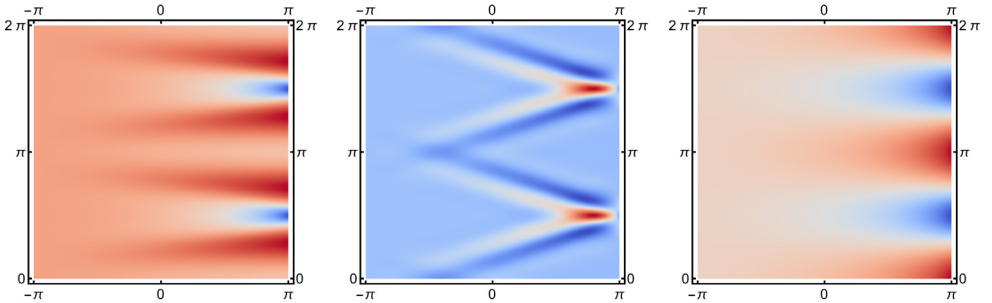

(a) $t = 1/100$ (b) $t = 1/100$ (c) $t = 1/100$

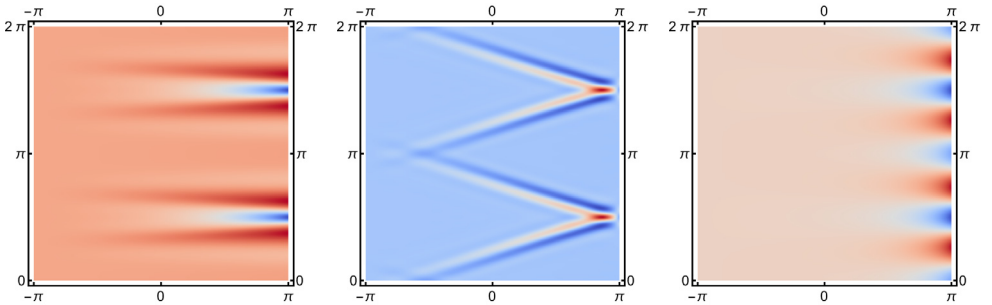

(d) $t = 1/1000$ (e) $t = 1/1000$ (f) $t = 1/1000$

Geometry	Profile	t	[Min,Max]
Parabolic	$f(x) = 1$	$1/100$	$[-0.431806, 0.158014]$
		$1/1000$	$[-1.94473, 0.756363]$
Hyperbolic	$f(x) = 1 + \frac{1}{2}\left(\frac{x}{\pi}\right)^2$	$1/100$	$[-0.133352, 0.29237]$
		$1/1000$	$[-0.415999, 0.860766]$
Elliptic	$f(x) = 1 - \frac{1}{2}\left(\frac{x}{\pi}\right)^2$	$1/100$	$[-6.00624, 4.51359]$
		$1/1000$	$[-91.7826, 68.9934]$

(g) Transverse deflections.

Fig. 4. Reference results for model geometries under symmetric concentrated load acting on u-component at the free boundary at $x = \pi$. [Min, Max] refers to transverse displacements. Columns from left: parabolic, hyperbolic, and elliptic.

4.2. Implementations

The first solver used in this study is implemented with Mathematica, providing exact geometry handling of the holes via blending functions [27]. The Naghdi results have been computed with this version.

The second one is AptoFEM, a parallel code implemented in FORTRAN90 and MPI. It allows for arbitrary order of polynomials to be used in the elements. Different order of polynomials can be used in different elements in the same mesh. Crucially, in order to minimise integration errors on complicated domains, the shape of the elements are represented using the transfinite interpolation method [28] which allows for the edges of the elements to be bent exactly to match the shape of the holes. Together with high order quadrature rules, the integration errors in the discrete problem are controlled. The code includes adaptivity in the form of estimation of the error η of the energy of the solution:

$$\eta := \sqrt{\mathcal{E}(\mathbf{u}_H - \mathbf{u}_h, \mathbf{u}_H - \mathbf{u}_h)}\,, \tag{10}$$

where $\mathbf{u}_H$ is the solution to be tested and $\mathbf{u}_h$ is the solution computed on a finer finite element space constructed completely and uniformly refining the mesh used for $\mathbf{u}_H$ and increasing the order p of polynomials by one in all elements. The same approach to estimating the error is used to drive the automatic mesh optimisation in [28].

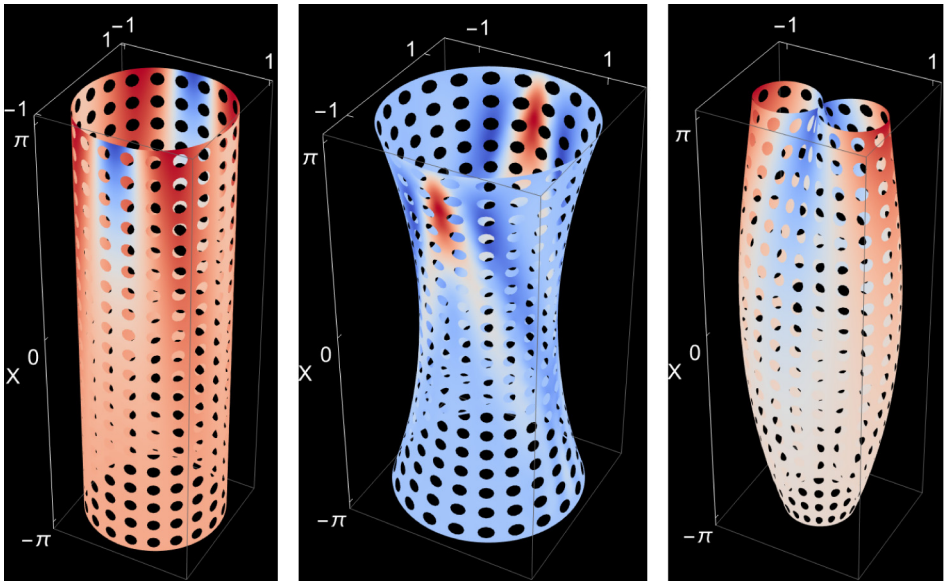

Fig. 5. Surface plots on regular perforations with deformations; $t = 1/100$. Scaling is not equal, elliptic scaling is adjusted to avoid self-intersection.

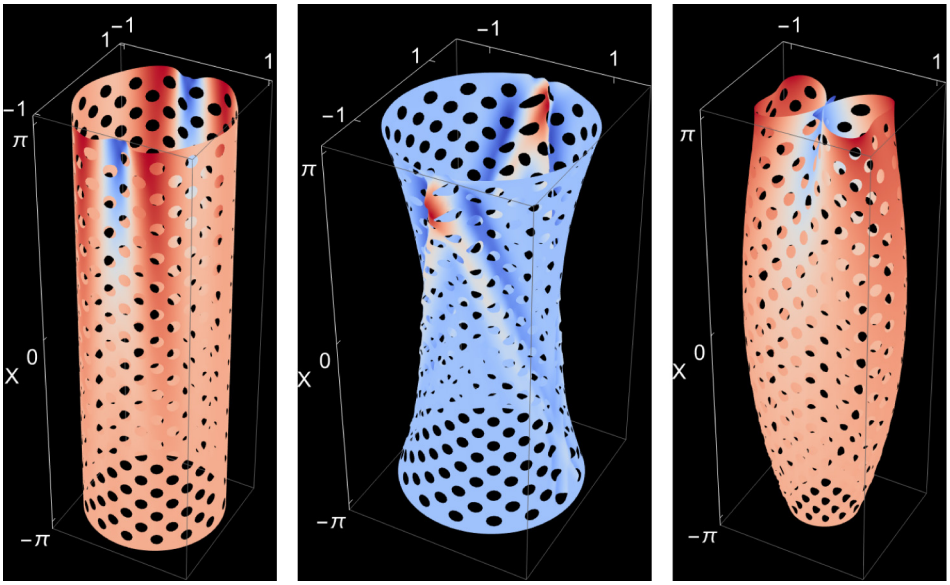

Fig. 6. Surface plots on triangular perforations with deformations; $t = 1/1000$. Scaling is not equal, elliptic scaling is adjusted to avoid self-intersection.

To reduce the computational time, the assembly of the linear system is done in parallel using MPI and the solution is computed in parallel using MUMPS [29–31] with MPI. This solver has been ported to Finnish supercomputers operated by the CSC as well as to the Aalto University cluster.

The shallow shell model results have been computed using AptoFEM with full adaptivity.

5. Numerical experiments: Computational asymptotic analysis

The numerical experiments can be divided into two sets depending on whether the geometry type is constant or not. The constant geometry types are simulated with the shallow shell model, but naturally the mixed geometry case with Naghdi.

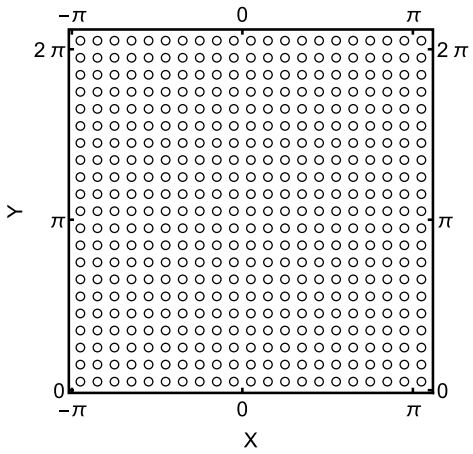

(a) Computational domain: $[-\pi, \pi] \times [0, 2\pi]$.

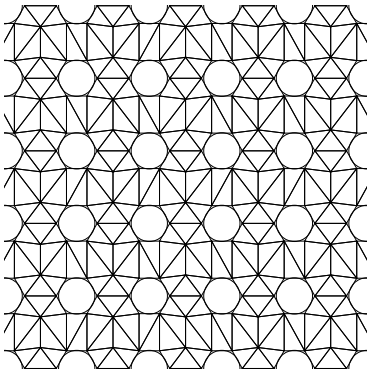

(b) Basic mesh.

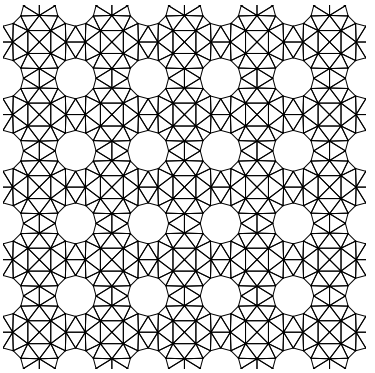

(c) Refined mesh.

Fig. 7. Computational domain with a regular 20 × 20-grid at 25% hole coverage. The boundary at $x = -\pi$ is clamped, $x = \pi$ is free. The other boundaries at $y = 0$ and $y = 2\pi$ are periodic. Two mesh details: The coarser mesh is used in adaptive solution, the finer one is used in Naghdi simulations without adaptivity.

Table 2
Overview of the experiments.

Category	Options
Geometry	Parabolic: $a = 0,\ b = 1,\ c = 0$ Hyperbolic: $a = 1,\ b = -1,\ c = 0$ Elliptic: $a = 1/2,\ b = 1,\ c = 0$ Mixed: See below.
Penetration pattern	Regular
Grid size	20
Hole coverage	25%
Thickness	Logarithmic division, 41 samples, $t \in [10^{-4}, 10^{-2}]$
Loading	Symmetric pinching acting on either u- or w-component.
Load locations	Two sets of rows aligned with the regular perforation pattern. Set A: 41 locations and Set B: 21 locations.

5.1. Experimental setup

The set of experiments is summarised in Table 2. Discretisation details are given in Fig. 7 and Table 3. The purpose of this study is to illustrate how different features are connected and how they interact, hence the perforation pattern is fixed to be the same in all experiments. Some variation might have resulted from the inclusion of triangular perforation

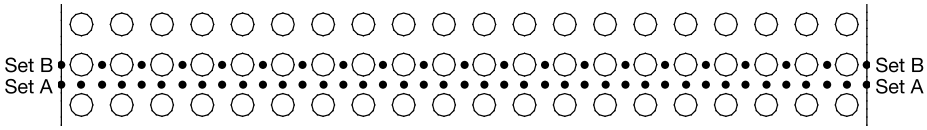

Fig. 8. Locations of the concentrated loads. Set A loads act on the area between the perforation rows, Set B loads act between the holes within the perforation row. In the figure the Set A and B locations are marked as the bottom and top rows of dots, respectively.

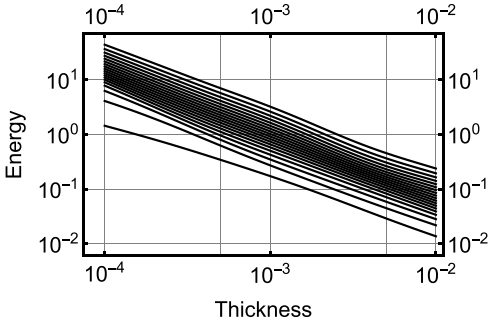

(a) Loading on w.

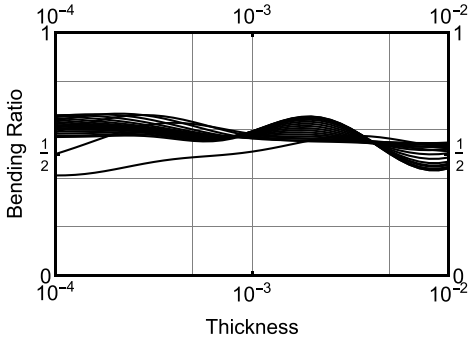

(b) Loading on w.

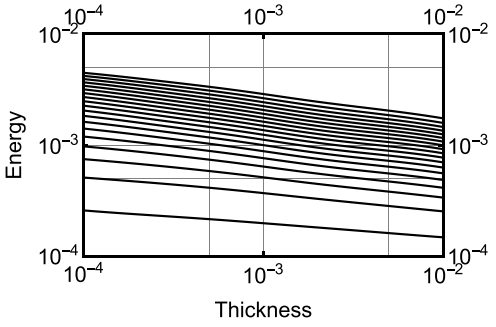

(c) Loading on u.

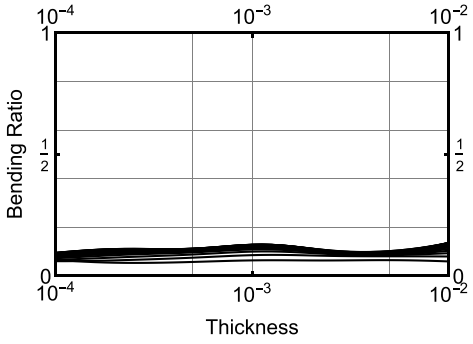

(d) Loading on u.

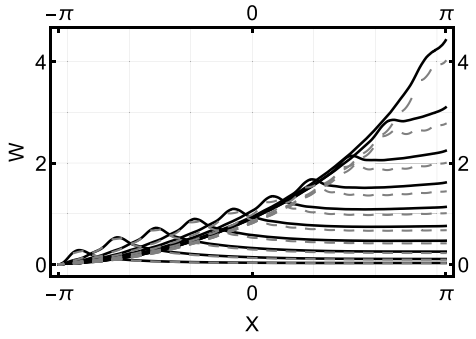

(e) $t = 1/100$.

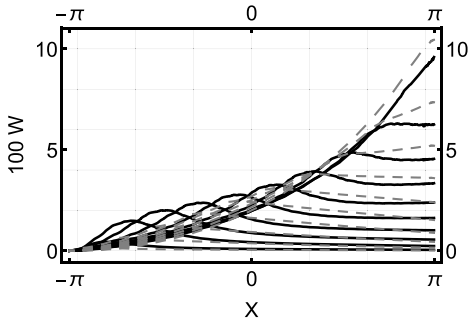

(f) $t = 1/10000$.

Fig. 9. Parabolic case. Effect of the load location to energy response and local transverse deflection profiles, (a)–(d) Set A. In (e) and (f) solid lines are Set A profiles and gray dashed (due to holes) ones Set B profiles. Notice that the local effects start dominating as $t \to 0$ and the maximal deflections are found within Set B in (f).

patterns, but it would have expanded the paper considerably. The model for the concentrated load is

$$f(x,y) = \exp(-100((x-x_0)^2 + (y-y_0)^2)) + \exp(-100((x-x_0)^2 + (y-(y_0+\pi)^2))), \tag{11}$$

Table 3
Data on discretisations. Meshes used in simulations and the number of degrees of freedom at uniform $p = 5$. Since both shell models considered here use the same domain parametrisation, the same mesh has been used for both if needed.

	%	g	Nodes	Edges	Triangles	DOF	Adapted
Basic	25	20	3636	9305	5270	362380	1979205
Refined	25	20	8681	22040	12960	873005	–

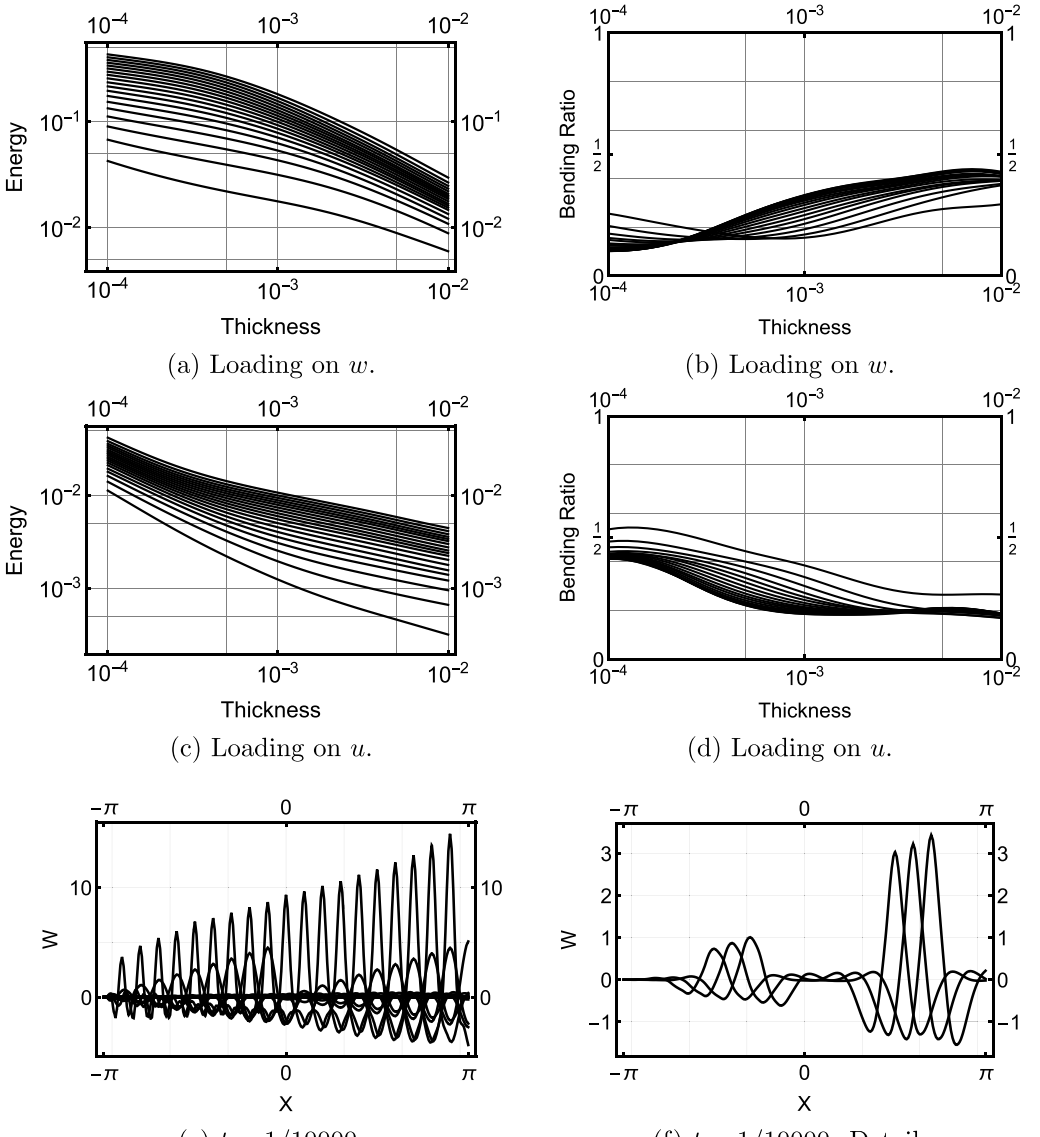

(a) Loading on w. (b) Loading on w.

(c) Loading on u. (d) Loading on u.

(e) $t = 1/10000$. (f) $t = 1/10000$. Detail.

Fig. 10. Hyperbolic case. Effect of the load location to energy response and local transverse deflection profiles, (a)–(d) Set A. In (e) it appears that the profiles are not only concentrated around the point of loading. This is illustrated in (f) in more detail. These secondary effects are caused by the internal layer emanating from the symmetric part of the loading.

where the point (x_0, y_0) is where the load acts, i.e., is concentrated. The distribution of loading points and the separation of them to Sets A and B is shown in Fig. 8. This choice of loads (or alternatively the points) is based on our earlier work on eigenproblems where these two regions play an important role. For a given configuration at some critical thickness t_c, the local features of the solution begin to dominate and the deflections due to Set B should have higher amplitudes than those of Set A at equal distance from the boundary. Notice that even though the basic mesh is rather coarse, the

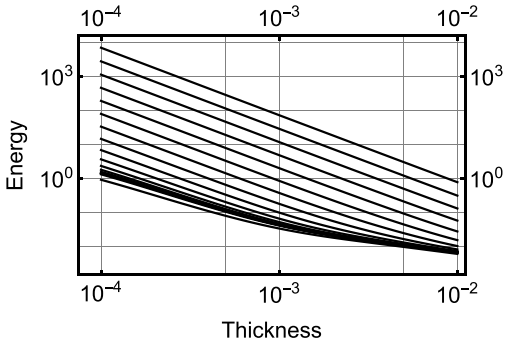

(a) Loading on w.

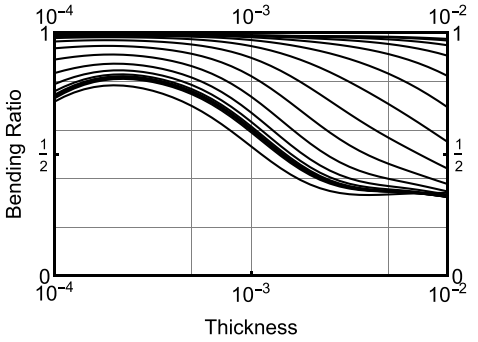

(b) Loading on w.

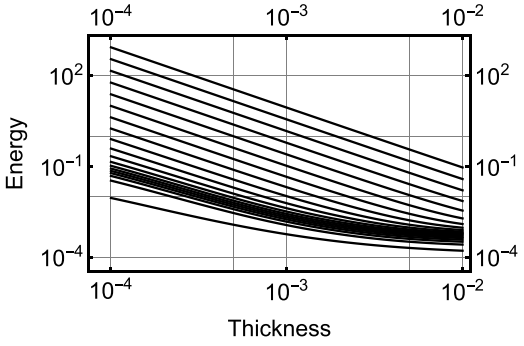

(c) Loading on u.

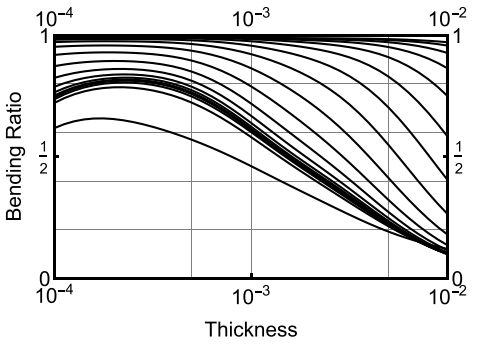

(d) Loading on u.

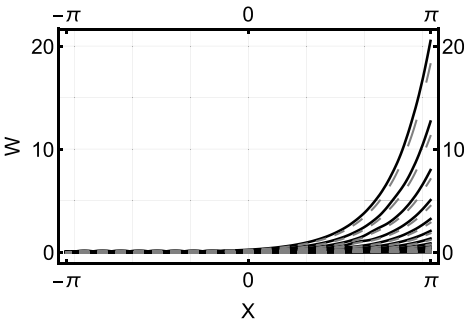

(e) $t = 1/100$.

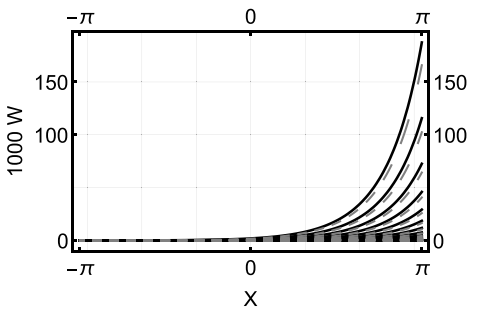

(f) $t = 1/10000$.

Fig. 11. Elliptic case. Effect of the load location to energy response and local transverse deflection profiles, (a)–(d) Set A. In (e) and (f) solid lines are Set A profiles and grey dashed (due to holes) ones Set B profiles. Notice that the Set A deflections dominate in both (e) and (f).

hp-adaptive step modifies it and the effective number of degrees of freedom is higher. The selection of $p = 5$ as the base level is related to avoidance of numerical locking in the sense of minimising the error, not the convergence rate.

In many figures below all cases of either Set A or Set B are included, for instance, in the energy response graphs. In most cases the trends based on the locations of the loads are clear and no attempt to identify individual cases has been made.

5.2. Layer effects

The first set of experiments focuses on the interaction between the perforation pattern and the layer structure. In Figs. 9, 10, and 11 the typical deformation profiles and energy convergence including the ratio of the bending energy of the total are shown for the parabolic, hyperbolic, and elliptic reference geometries, respectively. As one would expect the cases with axial pull lead to lower energy responses. The effect of the geometry on the ratio of the bending energy is evident. For the parabolic case, the axial pull leads to pure membrane state, whereas transverse loading results in a balance between bending and membrane stretching. The situation is somewhat reversed for the hyperbolic case with the

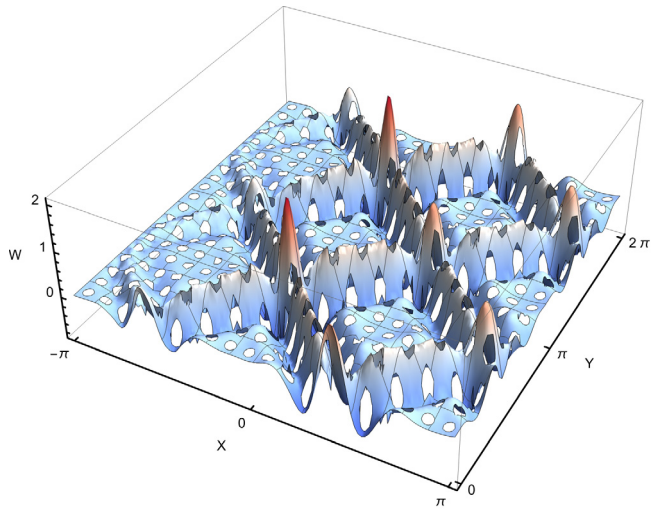

(a) Loading on w, $t = 1/1000$, at $x = -\pi/10$ (Set A).

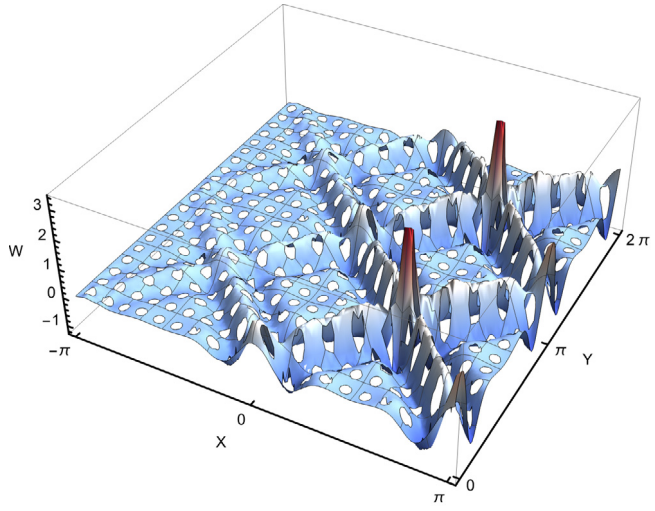

(b) Loading on w, $t = 1/1000$, at $x = \pi/2$ (Set B).

Fig. 12. Hyperbolic case (Transverse deflection plots): Examples of two concentrated loads connecting via internal layers reflected from the boundary.

axial pull resulting in slightly higher relative amount of bending. Of course, the elliptic case is bending-dominated once the loads start acting away from the clamped boundary. The transverse deflection profiles for the parabolic show the expected phenomenon that for $t = 1/100$ the Set A leads to higher amplitudes, but at $t = 1/1000$ the local features due to boundary layers around the holes begin to dominate and the Set B (dashed lines in the figure) has the highest amplitudes. In elliptic cases the transverse deflection profiles are very similar whether one considers either Set A or Set B. However, in the hyperbolic case there appears to be an unexpected effect along the axis far away from the concentrated load.

This feature in the hyperbolic case is a result of the locations of the concentrated loads, thickness, and the perforation pattern being in perfect alignment for a superposition of the internal layers to occur. This is illustrated in Fig. 12. In fact, in Fig. 12(a) there are multiple crossings of the internal layers each with local superposition. In Fig. 12(b) the superposition occurs when the layers are pseudo-reflected from the boundary, and this reflection leads to the two loads amplifying each other.

5.3. Sensitive elliptic boundary oscillations

Some deflection patterns in the angular direction (constant axial coordinate) are shown in Fig. 13. In all cases the relative widths of the oscillations at a given thickness do not depend on the location of the load, only the amplitude does. Also, the hyperbolic layer is narrower than the parabolic one as the theory predicts.

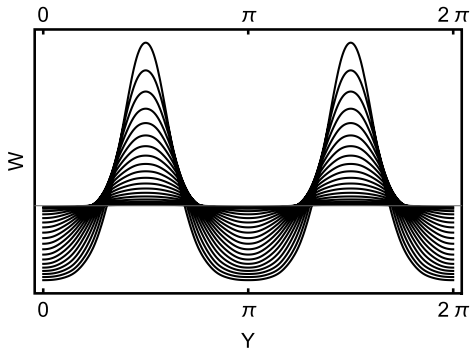

(a) Parabolic: Loading on w, $t = 1/100$.

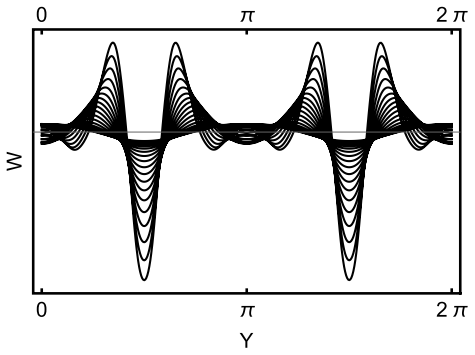

(b) Parabolic: Loading on u at $x = 0$.

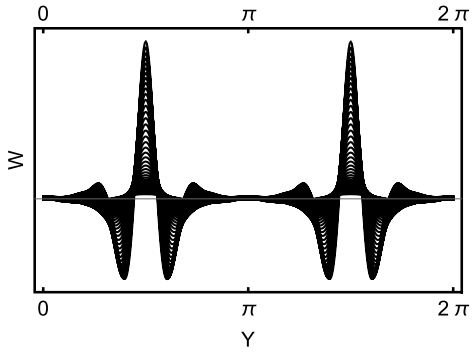

(c) Hyperbolic: Loading on w at $x = 0$, $t = 1/100$.

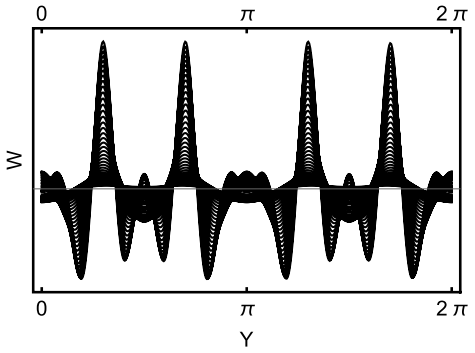

(d) Hyperbolic: Loading on w at $x = -4\pi/5$.

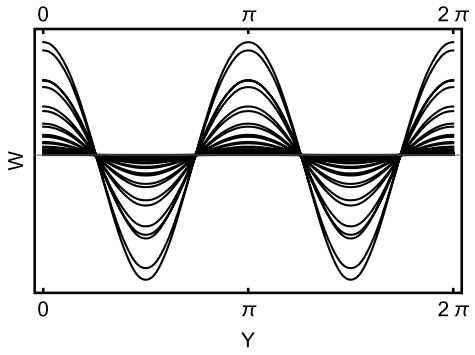

(e) Elliptic: Loading on u, $t = 1/1000$.

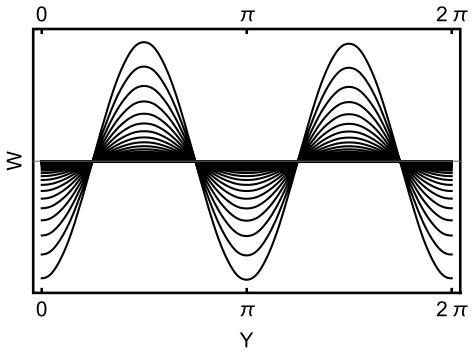

(f) Elliptic: Loading on w at $x = -4\pi/5$.

Fig. 13. Boundary oscillations.

The predicted wave number for oscillations at the free boundary in the elliptic case is $K \sim -\log t$. Interestingly, at first it appears that this feature is not observed in the experiments. However, there are two factors that have to be taken into account. First, the loading is symmetric and hence only even wave numbers can be observed, and second, the shallow shell model is computed on an idealised surface. In Fig. 14 the normalised transverse deflection profiles for $t = 10^{-k}$, $k = 2, 3, 4, 5, 6$, are shown for both shallow shell model and Naghdi. The geometry approximation leads to the shallow shell model being less sensitive than Naghdi, yet eventually the higher oscillations appear, although at thicknesses below the practical range.

5.4. Mixed geometry designs

The results above can be extended to cover cases with non-uniform Gaussian curvature. The first profile function is a hyperbolic tangent and the second one a piecewise linear function, that is, locally parabolic (See Fig. 15). Notice, that

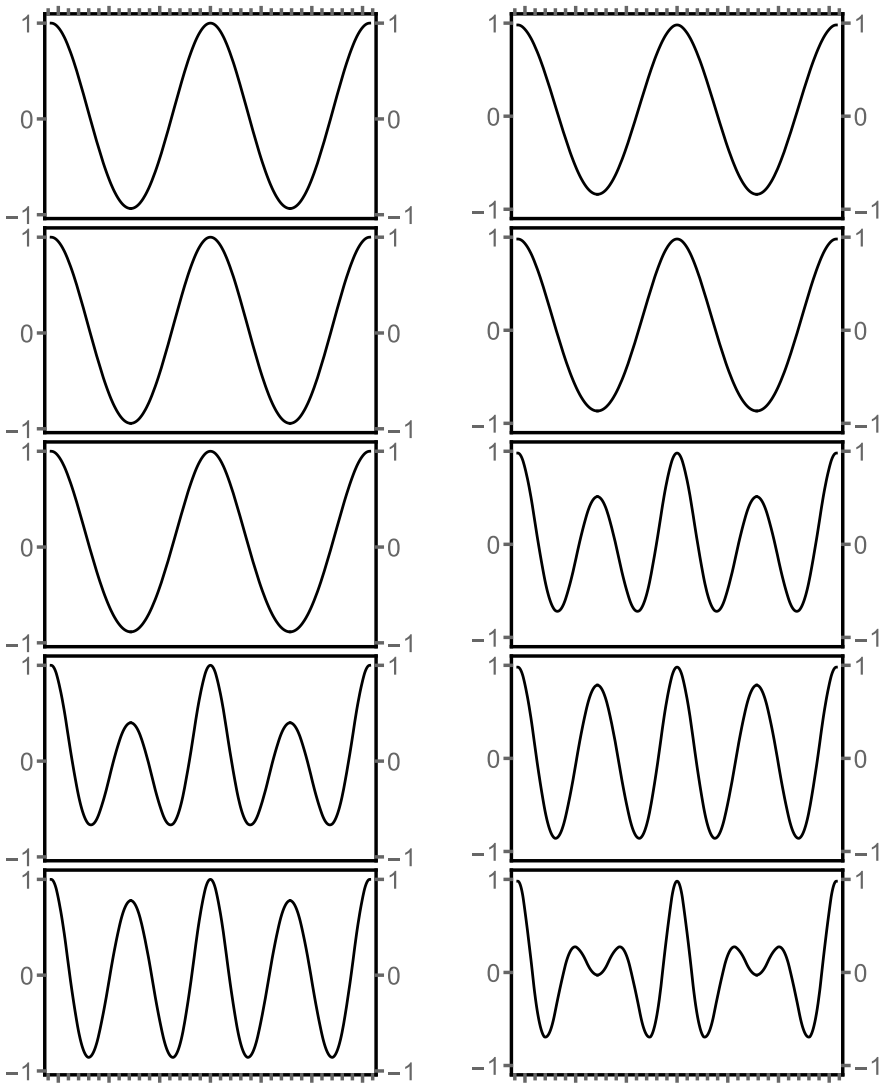

(a) Shallow Shell (b) Naghdi

Fig. 14. Normalised elliptic boundary oscillations with symmetric pinching on w-component. From top to bottom $t = 10^{-k}$, $k = 2, 3, 4, 5, 6$. Observed dominant wave numbers: (a) Shallow shell model: 2, 2, 2, 4, 4, (b) Naghdi: 2, 2, 4, 4, 6. Wave numbers must be even due to the symmetry of the loading..

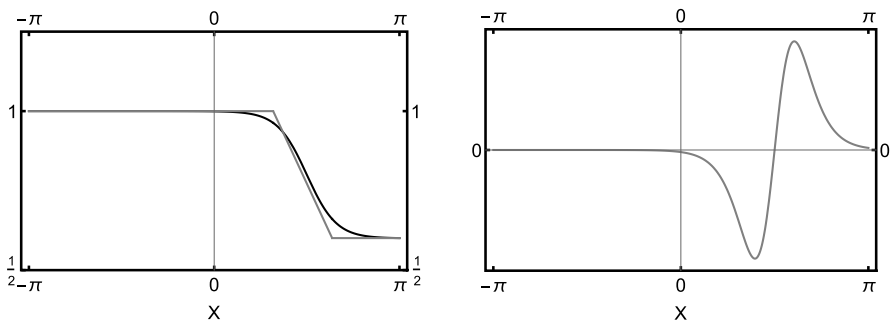

(a) Smooth and piecewise linear profiles. (b) Second derivative of the smooth profile.

Fig. 15. Mixed geometry profiles. The piecewise linear profile is parabolic over every segment. The smooth profile (hyperbolic tangent) includes regions with all three geometries.

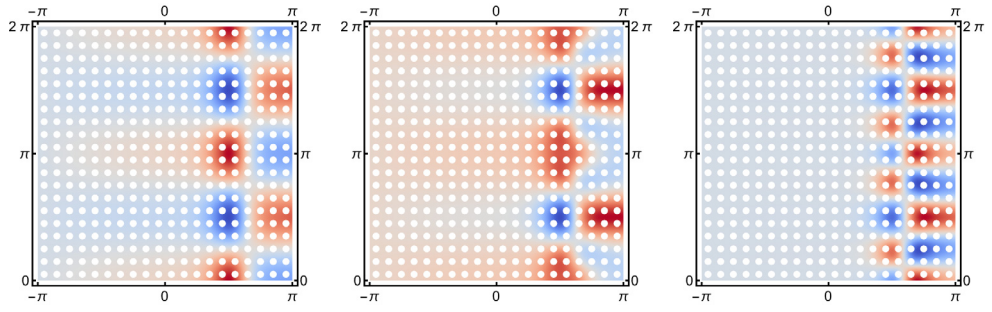

(a) Smooth: $t = 1/100$. (b) $t = 1/1000$. (c) $t = 1/10000$.

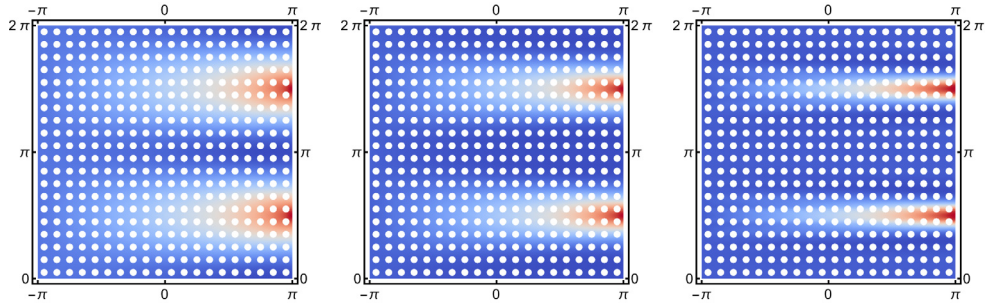

(d) Piecewise linear: $t = 1/100$. (e) $t = 1/1000$. (f) $t = 1/10000$.

Profile $f(x) =$		t	Energy
$\frac{4}{5} - \frac{1}{5}\tanh\left(2\left(x - \frac{\pi}{2}\right)\right)$			
		$1/100$	4.29797×10^{-4}
		$1/1000$	1.47604×10^{-3}
		$1/10000$	3.66942×10^{-2}
$\begin{cases} 1 & x < 1 \\ (x-1)\left(-\frac{1}{5} - \frac{\tanh(\pi)}{5}\right) + 1 & 1 \le x \le 2 \\ \frac{4}{5} - \frac{\tanh(\pi)}{5} & x > 2 \end{cases}$			
		$1/100$	1.79467×10^{-4}
		$1/1000$	2.94180×10^{-4}
		$1/10000$	4.64434×10^{-4}

(g) Transverse deflections.

Fig. 16. Experiments with non-uniform curvature profiles.

are committing a modelling crime here. The locally parabolic profile does not satisfy the smoothness assumptions used in the dimension reduction. However, the geometry parameters are only evaluated at the quadrature points and hence the ambiguity of the normal direction at $x = 1$ and $x = 2$ are avoided numerically. In other words, this way the profile is smoothened in a way that is implicit and not directly controllable. Hyperbolic tangent of course can be scaled to include regions of all three geometry types. Rather remarkably in the context of perforated sensitive shells it appears that inclusion of an elliptic region is enough to induce high energy responses as is evident in Fig. 16.

Notice that the concentrated load is not acting on the elliptic region. The singularity is propagated first along the parabolic part, and then along the characteristic curves of the hyperbolic section before activating the elliptic response.

6. Conclusions

Sensitive shells are a class of constructions with specific and perhaps unintuitive responses to different loading scenarios. There are new emerging applications for capsules with open cavities, and it is inevitable that as the boundaries of manufacturing are pushed to maximise the payload, the phenomena observed here become realistic. Of course, in the elliptic case linear elasticity is no longer valid in the limit case and in practical setting the construction simply fails.

The effect of the perforation patterns is perhaps surprisingly mild. Interestingly, in the mixed geometry case the responses of the piecewise linear and smooth function profiles were far apart. This suggests an area of future research: Is there a critical width of the elliptic part of the profile below which the elliptic part does not dominate the solution? Using current printing technologies, for instance, it is difficult to see how this region could be completely avoided.

The effects of the symmetric pinching observed in the hyperbolic case have not been reported in the literature before. Another question for future work arises immediately: What happens in frequency response analysis at the crossings? Could there be long-distance effects with larger amplitudes far away from the concentrated load?

Data availability

No data was used for the research described in the article.

Acknowledgement

We would like to thank an anonymous referee for valuable comments that improved the quality of the paper.

References

[1] V.-V. Auvinen, J. Virtanen, A. Merivaara, V. Virtanen, P. Laurén, S. Tuukkanen, T. Laaksonen, Modulating sustained drug release from nanocellulose hydrogel by adjusting the inner geometry of implantable capsules, J. Drug. Deliv. Sci. Technol. 57 (2020) 101625, http://dx.doi.org/10.1016/j.jddst.2020.101625.
[2] J.D. Yuen, L.C. Shriver-Lake, S.A. Walper, D. Zabetakis, J.C. Breger, D.A. Stenger, Microbial nanocellulose printed circuit boards for medical sensing, Sensors 20 (7) (2020) http://dx.doi.org/10.3390/s20072047.
[3] T. Laaksonen, Personal Communication, 2022.
[4] E. Sanchez-Palencia, O. Millet, F. Béchet, Singular Problems in Shell Theory, Springer-Verlag Berlin Heidelberg, 2010.
[5] S. Giani, H. Hakula, On effects of perforated domains on parameter-dependent free vibration, J. Comput. Appl. Math. 394 (2021) http://dx.doi.org/10.1016/j.cam.2021.113526.
[6] S. Giani, H. Hakula, Free vibration of perforated cylindrical shells of revolution: Asymptotics and effective material parameters, Comput. Methods Appl. Mech. Engrg. Online (2022).
[7] J. Pitkäranta, E. Sanchez-Palencia, On the asymptotic behaviour of sensitive shells with small thickness, Comptes Rendus de l'Académie des Sci. - Series IIB 325 (3) (1997) 127–134, http://dx.doi.org/10.1016/S1251-8069(97)86827-3.
[8] K.-J. Bathe, D. Chapelle, P.-S. Lee, A shell problem 'highly sensitive' to thickness changes, Internat. J. Numer. Methods Engrg. 57 (8) (2003) 1039–1052, http://dx.doi.org/10.1002/nme.708.
[9] E. Artioli, L. Beirão da Veiga, H. Hakula, C. Lovadina, On the asymptotic behaviour of shells of revolution in free vibration, Comput. Mech. 44 (1) (2009) 45–60.
[10] M. Chaussade-Beaudouin, M. Dauge, E. Faou, Z. Yosibash, High frequency oscillations of first eigenmodes in axisymmetric shells as the thickness tends to zero, in: Recent Trends in Operator Theory and Partial Differential Equations, Springer International Publishing, 2017, pp. 89–110, http://dx.doi.org/10.1007/978-3-319-47079-5_5.
[11] C.A. Schenk, G.I. Schuëller, Uncertainty assessment of large finite element systems, in: Lecture Notes in Applied and Computational Mathematics, vol. 24, Springer, 2005.
[12] H. Wang, J. Guilleminot, B. Shafer, M. Tootkaboni, Stochastic analysis of geometrically imperfect thin cylindrical shells using topology-aware uncertainty models, Comput. Methods Appl. Mech. Engrg. 393 (2022) 114780, http://dx.doi.org/10.1016/j.cma.2022.114780.
[13] D.J. Benson, Y. Bazilevs, M.C. Hsu, T.J.R. Hughes, Isogeometric shell analysis: The Reissner–Mindlin shell, Comput. Methods Appl. Mech. Engrg. 199 (5–8) (2010) 276–289, http://dx.doi.org/10.1016/j.cma.2009.05.011.
[14] J. Pitkäranta, A.-M. Matache, C. Schwab, Fourier mode analysis of layers in shallow shell deformations., Comput. Methods Appl. Mech. Engrg. 190 (2001) 2943–2975.
[15] P.M. Naghdi, Foundations of elastic shell theory, in: Progress in Solid Mechanics, vol. 4, North Holland, 1963, pp. 1–90.
[16] M. Malinen, On the classical shell model underlying bilinear degenerated shell finite elements: General shell geometry, Internat. J. Numer. Methods Engrg. 55 (6) (2002) 629–652.
[17] J. Pitkäranta, The problem of membrane locking in finite element analysis of cylindrical shells, Numer. Math. 61 (1992) 523–542.
[18] H. Hakula, Y. Leino, J. Pitkäranta, Scale resolution, locking, and high-order finite element modelling of shells, Comput. Methods Appl. Mech. Engrg. 133 (1996) 157–182.
[19] B. Szabo, I. Babuska, Finite Element Analysis, Wiley, 1991.
[20] C. Schwab, *p*- and *hp*-Finite Element Methods, Oxford University Press, 1998.
[21] S. Bieber, B. Oesterle, E. Ramm, M. Bischoff, A variational method to avoid locking – independent of the discretization scheme, Numer. Methods Eng. 114 (8) (2018) 801–827.
[22] Y. Ko, P.-S. Lee, K.-J. Bathe, A new MITC4+ shell element, Comput. Struct. 182 (2017) 404–418.
[23] T. Ho-Nguyen-Tan, H.-G. Kim, Polygonal shell elements with assumed transverse shear and membrane strains, Comput. Methods Appl. Mech. Engrg. 349 (2019) 595–627.
[24] M. Do Carmo, Differential Geometry of Curves and Surfaces, Prentice Hall, 1976.
[25] A.H. Niemi, J. Pitkäranta, Bilinear finite elements for shells: Isoparametric quadrilaterals, Internat. J. Numer. Methods Engrg. 75 (2) (2008) 212–240, http://dx.doi.org/10.1002/nme.2252.
[26] M. Malinen, J. Pitkäranta, A benchmark study of reduced-strain shell finite elements: Quadratic schemes, Internat. J. Numer. Methods Engrg. 48 (11) (2000) 1637–1671, http://dx.doi.org/10.1002/1097-0207(20000820)48:11{<}1637::AID-NME954{>}3.0.CO;2-H.

[27] H. Hakula, T. Tuominen, Mathematica implementation of the high order finite element method applied to eigenproblems, Computing 95 (1) (2013) 277–301, http://dx.doi.org/10.1007/s00607-012-0262-4.
[28] P. Solin, K. Segeth, I. Dolezel, Higher Order Finite Element Methods, Har/Cdr ed., Chapman and Hall/CRC, 2003.
[29] P.R. Amestoy, I.S. Duff, J.-Y. L'Excellent, Multifrontal parallel distributed symmetric and unsymmetric solvers, Comput. Methods Appl. Mech. Engrg. 184 (2000) 501–520.
[30] P.R. Amestoy, I.S. Duff, J. Koster, J.-Y. L'Excellent, A fully asynchronous multifrontal solver using distributed dynamic scheduling, SIAM J. Matrix Anal. Appl. 23 (2001) 15–41.
[31] P.R. Amestoy, A. Guermouche, J.-Y. L'Excellent, S. Pralet, Hybrid scheduling for the parallel solution of linear systems, Parallel Comput. 32 (2006) 136–156.